Proteome constrained metabolic modeling of *Sus scrofa* muscle stem cells for cultured meat production

Authorship

Sizhe Qiu[1,2‡], Eliska Kratochvilova[1,2‡], Wei E. Huang[1], Zhanfeng Cui[1,2], Tom Agnew[3], Aidong Yang[1*], Hua Ye[1,2*]

[1]Department of Engineering Science, University of Oxford, OX1 3PJ, United Kingdom

[2]Institute of Biomedical Engineering, Department of Engineering Science, University of Oxford, Oxford OX3 7DQ, United Kingdom

[3]Ivy Farm Technologies, OX4 2GX, United Kingdom

[‡]Equal contribution

*Corresponding author: aidong.yang@eng.ox.ac.uk (A. Yang), hua.ye@eng.ox.ac.uk (H. Ye)

Keywords

Cultured meat; *Sus scrofa*; Stem cell; Metabolic model; Constrained proteome allocation;

Abstract

Cultured meat has recently emerged as a sustainable alternative to traditional livestock farming and gained attention as a promising future protein source. Herein, the *Sus scrofa* muscle stem cell is a commonly used cell source in the cell proliferation step of cultured meat production. However, a major bottleneck of large-scale cultivation is the inhibition by secreted and accumulated lactate and ammonium in the process of *S. scrofa* cell proliferation. To simulate the growth and metabolism of *S. scrofa* muscle stem cells under different lactate and ammonium concentrations, this study constructed the first proteome constrained metabolic model for the core metabolism of *S. scrofa* muscle stem cells, pcPigMNet2025. The relationship of lactate and ammonium levels with cellular metabolism was derived from growth and metabolomics data of two culture conditions with low and high initial ammonium concentrations, and then incorporated into metabolic flux simulation. Metabolic flux simulations for experimental conditions, along with perturbation simulations considering stressed non-growth associated maintenance and oxygen supply, demonstrated that pcPigMNet2025 could effectively characterize the response of the *S. scrofa* muscle stem cell's growth and metabolism to varying environmental conditions, shedding light on model-aided control and optimization of the cultured meat production process.

Graphical abstract

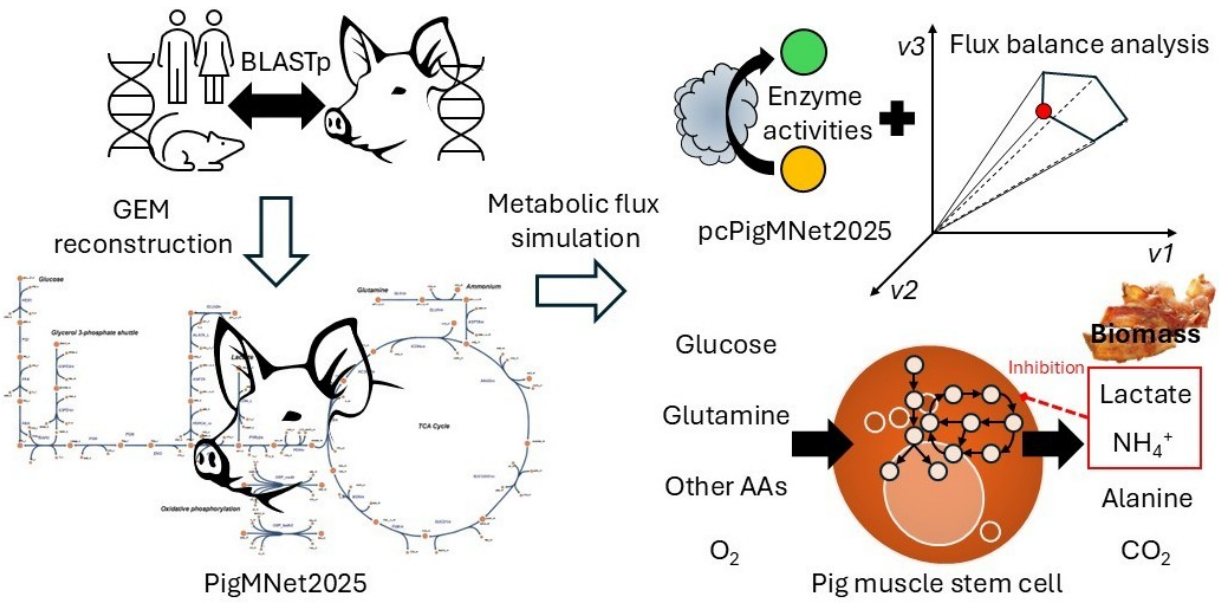

Highlights

1. The first proteome constrained metabolic model was built for *S. scrofa* myoblasts.
2. This model effectively simulated myoblast metabolism under lactate and NH_4^+ stress.
3. Perturbation simulations showed that this model could also account for other stress.
4. This model enables *in-silico* control and optimization of cultured meat production.

Abbreviations

CHO: Chinese hamster ovary; DCW: dry cellular weight; DW: dry weight; GAM: growth associated maintenance; GEM: genome-scale metabolic model; GPR: gene-protein-reaction rule; FBA: flux balance analysis; NGAM: non-growth associated maintenance; NH_4^+: ammonium; OUR: oxygen uptake rate; RMM: reduced metabolic model; TCA: tricarboxylic acid;

3

1.Introduction

With the rapidly increasing global consumption of meat (Godfray et al., 2018), the traditional livestock farming has placed a growing burden on the environment (Tullo et al., 2019), such as increased land demand, carbon dioxide emission (Caro et al., 2014), and water pollution (Yang et al., 2020). Consequently, cultured meat production from mammalian stem cells has been considered as a sustainable alternative, and the *Sus scrofa* (pig) muscle stem cell is one of the most commonly used cell sources (M. Li et al., 2022; Post, 2012; Zhu et al., 2022). In cultivated pork production, the cell proliferation (biomass production) in the bioreactor is the determining step of cultured meat yield, but the inhibition of cellular growth by secreted and accumulated lactate and ammonium (NH_4^+) becomes the bottleneck (Chen et al., 2009; Hassell et al., 1991; Ryll et al., 1994; Slivac et al., 2010). As major products of central carbon metabolism and amino acid metabolism, lactate and NH_4^+ in mammalian cell culture limits cellular growth in a feed-back mode. Therefore, a predictive model of the *S. scrofa* muscle stem cell's metabolism is desirable to characterize its interactions with the growth environment in the bioreactor for the quantitative analysis and control of cultured meat production process.

Regarding cellular metabolism, flux balance analysis (FBA) with genome scale metabolic models (GEMs) is a widely-used computational method to predict metabolic fluxes under different conditions (Orth et al., 2010). Compared to differential equation-based metabolic models, FBA offers advantages in interpretability and computational efficiency (Qiu et al., 2023a). In recent years, researchers have already built GEMs for several well-studied animal species (Wang et al., 2021). The representative ones are iCHO for Chinese hamster ovary (CHO) cells (Hefzi et al., 2016), RECON1 and RECON-3D for human metabolism (Duarte et al., 2007), and BtaSBML2986 for bovine satellite cells in cultured meat production (Lee et al., 2024). Hence, GEM reconstruction is a feasible approach to analyze the metabolism of *S.*

scrofa muscle stem cells. With respect to metabolic flux simulation, Nolan and Lee, 2011 combined differential equation-based kinetics and FBA to dynamically model CHO cell metabolism with changing metabolite concentrations (Nolan and Lee, 2011); Yeo et al., 2020 incorporated enzyme kinetic information into iCHO and adopted the enzyme capacity constrained FBA framework (Shlomi et al., 2011) to achieve accurate flux prediction (Yeo et al., 2020). However, none of these models has incorporated the influence of environmental factors (e.g., the accumulation of lactate) which exist in actual bioprocesses.

With the objective to simulate *S. scrofa* muscle stem cell proliferation under different lactate and NH_4^+ levels, this study attempted to construct the first proteome constrained FBA model for *S. scrofa* muscle stem cells, pcPigMNet2025. By approximating the inhibitory effects of lactate and NH_4^+ using measured growth and extracellular metabolomics data, this study managed to incorporate major environmental stress factors in *S. scrofa* muscle stem cell culture into metabolic flux simulation. Subsequently, the accuracy of pcPigMNet2025 was evaluated through validation against experimental data. Overall, this study intended to present pcPigMNet2025 as a metabolic modeling framework with the potential to be a model-aided process engineering tool for controlling and optimizing cultured meat production.

2.Materials and methods

2.1 Culture conditions of *S. scrofa* muscle stem cells

Genetically engineered, immortalised, suspension-adapted skeletal-muscle derived stem cells (*S. scrofa*, obtained from Ivy Farm Technologies, Oxford, UK, under a material transfer agreement) were cultured in SR7 medium (formulation by Ivy Farm Technologies, Oxford, UK) supplemented with 1% (v/v) penicillin–streptomycin. The formulation of SR7 medium is based on DMEM/F-12 supplemented with amino acids, lipid concentrate, nucleosides, AlbuMAX, poloxamer 188, anti-clumping agent, fetal bovine serum (FBS) growth factors and others. The

exact composition of SR7 medium and the detailed cell culture handling protocols were provided by Ivy Farm Technologies and are proprietary to the company.

Stem cell cultures were maintained at 37 °C in a humidified incubator with 5% CO_2, in baffled Erlenmeyer flasks with vented filter lids, with the working volume set to one-fifth of flask capacity, and agitated on an orbital shaker (SSM1, Stuart, UK) at 140 rpm for cultures ≤50 mL and 120 rpm for cultures ≥100 mL. For the low initial NH_4^+ culture experiment, cells at passage 59 were grown in 50 mL SR7 medium at 140 rpm. On day 3, the pre-stationary cultures were seeded into three flasks containing 110 mL medium at a density of 1.0×10^5 cells/mL and incubated at 120 rpm. Because cells were transferred from pre-existing confluent cultures, a small volume of conditioned medium was unavoidably carried over, resulting in low but non-zero initial concentrations of NH_4^+ and lactate. For the high initial NH_4^+ culture experiment, SR7 medium was supplemented with ammonium chloride (NH_4Cl) to a final concentration of 3.5 mM. Cells at passage 64 (two cultures of 25 mL each, 140 rpm), likewise in pre-stationary phase, were seeded on day 3 into three flasks containing 110 mL medium at a density of 1.0×10^5 cells/mL and incubated at 120 rpm.

At every sampling point, 1 mL samples were withdrawn from each flask and centrifuged at 600 × g for 5 min at room temperature. The resulting cell pellets were treated with TrypLE (Thermo Fisher Scientific, UK) at 37 °C for 5 min, neutralised with fresh medium to the original volume, and mixed 1:1 with 0.4% Trypan Blue Stain (Thermo Fisher Scientific, UK). Cell counts were obtained using an automated cell counter (Countess™, Thermo Fisher Scientific, UK), with each biological replicate value representing the mean of at least two independent technical measurements.

2.2 Metabolomics analysis of *S. scrofa* muscle stem cell culture

Following centrifugation, supernatants were collected for metabolomics analysis and stored at ultra-low temperature (−80 °C or liquid nitrogen) for no longer than one week prior to analysis. Freezing protocols (−80 °C or liquid nitrogen) were selected based on equipment availability. The measured analytes in this study (glucose, lactate, glutamine, NH_4^+) are stable under frozen storage (Wagner-Golbs et al., 2019), and the metabolic activity is fully quenched.

Glucose, lactate, glutamine and NH_4^+ concentrations were measured using a Nova Flex 2 analyser (Nova Biomedical, UK). The pH was measured at room temperature using a glass combination pH electrode (InLab Micro, Mettler Toledo, UK), calibrated before each measurement session. For both low and high initial NH_4^+ level conditions, the pH was maintained to be around 7.5, a slightly alkaline pH (**see Figure S1 in SI**). For each metabolite concentration measurement, there were three biological replicates (three independent flasks). The analytical workflow was adapted from the metabolomics profiling of CHO cells (Széliová et al., 2020), with modifications for *S. scrofa* myoblasts. Cell-specific uptake rates of glucose, glutamine, oxygen and production rates of lactate, NH_4^+ were computed using measured metabolite concentrations and cell counts at different time points (**see section S1.1 and Figure S2 in SI**).

2.3 Reduced metabolic model reconstruction of *S. scrofa* muscle stem cell

To build the genome-scale metabolic model (GEM) of the *S. scrofa* muscle stem cell, bidirectional BLASTp (Camacho et al., 2009) was used to find homologous proteins for metabolic reactions and then curate gene-protein-reaction rules (GPRs) from template GEMs. RECON1 (*Homo sapiens*) (Duarte et al., 2007) and iCHO (*Cricetulus griseus*) (Hefzi et al., 2016) were used as template genome-scale metabolic models (GEMs). The template genomes

of *S. scrofa*, *H. sapiens*, and *C. griseus* used in this study were GCF_000003025.6, GCF_000001405.33, and GCF_003668045.3, respectively. For bidirectional BLASTp, the threshold of e-value was 1e-6, and over 93% of matched homologous proteins had e-values < 1e-20 (**see Figure S6 in SI**). With matched homologous proteins, metabolic reactions were curated based on the boolean computation of GPRs (e.g., GPR="A or B", the existence of either gene A or B will include the reaction; GPR="A and B", the reaction can only be included if both gene A and B exist). Boundary reactions were added for all metabolites in the extracellular space. The biomass formation reaction (default objective function) was modified from the one in iCHO, based on the experimental measurement of *S. scrofa*'s cellular biomass composition (**see section S1.2 in SI**). The growth associated maintenance (GAM) and non-growth associated maintenance (NGAM) values were estimated using approximated cell-specific ATP generation rates and growth rates (**see Figure S3 in SI**). For metabolic network gap-filling, transportation reactions of organelles and pseudo biosynthetic reactions with no GPR associated were manually added from RECON1 and iCHO to ensure all components in the biomass composition can be produced in FBA. Redundant metabolites and reactions were manually removed.

To facilitate the integration of enzyme activities (**section 2.4**) and improve model interpretability, this study built a reduced metabolic model (RMM) based on the GEM of the *S. scrofa* muscle stem cell, namely PigMNet2025. Only reactions in the subsystems of glycolysis, pentose phosphate pathway, tricarboxylic acid (TCA) cycle, oxidative phosphorylation, amino acid metabolism, urea cycle, nucleotide metabolism, and lipid synthesis were included in this RMM. Metabolites and reactions in the compartments of nucleus, peroxisome/glyoxysome, lysosome, and endoplasmic reticulum were removed. The quality of the finalized RMM of the *S. scrofa* muscle stem cell was assessed by MEMOTE (Lieven et al., 2020), and the MEMOTE report can be found at

https://github.com/SizheQiu/PigMNet2025/data/gems/memote_report.html. Escher was used to visualize the metabolic network (King et al., 2015).

2.4 Proteome constrained flux balance analysis of *S. scrofa* muscle stem cells

To tighten the metabolic flux solution space, this study integrated proteome constraints of reactions into conventional FBA (Orth et al., 2010) to build a proteome constrained FBA model (Mori et al., 2016) for *S. scrofa* muscle stem cells, namely, pcPigMNet2025. COBRApy (Ebrahim et al., 2013) was used to perform FBA. The objective function was maximization of the growth rate (μ) (Eq. 1), and the default constraint was mass conservation (Eq. 2). S is the stoichiometric matrix of the metabolic reaction network, and v represents the vector of reaction fluxes (Eq. 2). The proteome of *S. scrofa* was divided into five sectors: C sector for carbon catabolism, E sector for biosynthesis of amino acids, lipids, nucleotides, and polysaccharides, A sector for anabolism (biomass formation), T sector for transporter proteins, and O sector for proteins not belonging to core cellular metabolism. Enzymes and enzyme-catalyzed reactions were grouped into A, C, E, and T sectors based on their annotated metabolic subsystems (e.g., glycolysis for the C sector). ϕ_j represented the mass fraction of the sector j for $j = A, C, E, T, O$, and the mass fractions of all five sectors summed to 100% (Eq. 3). $\phi_O \geq \phi_{O,min}$, and the value of $\phi_{O,min}$ was estimated to be 0.5953 (**see Figure S4 in SI**). For enzyme-catalyzed reactions, the reaction flux (v_i, $\frac{mmol}{hr * gDW}$) was constrained by the enzyme activity, $a_i(\frac{mmol}{hr * g\,E})$ (Eq. 4). Enzyme activity quantifies the amount of substrate converted per unit of time per unit of enzyme mass, and enzyme activity values were obtained from BRENDA (Chang et al., 2021) and SABIO-RK (Wittig et al., 2018). For enzymes without activity values measured for *S. scrofa*, this

9

study chose the largest enzyme activity value from data entries of mammalian species genetically close to *S. scrofa* (e.g., *H. sapiens*). The details of enzyme activity values can be found in **SI, Table S6**. Therefore, the fluxes of enzyme-catalyzed reactions belonging to A, C, E, T sectors were constrained by enzyme activity values and proteome sector mass fractions (Eq. 5). P_{TOT} was the total mass of the proteome normalized to 1 gDW of biomass ($\frac{g}{gDW}$) (**see Table S3 in SI**).

Eq. 6-8 were integrated into FBA to model the inhibitory effects of lactate and NH_4^+. $ub_{glucose}$, $ub_{glutamine}$, and ub_{O_2}were upper bounds of uptake fluxes of glucose, glutamine, and oxygen. Eq. 7 was also applied to the upper bounds of uptake fluxes of other amino acids. Eq. 6 was a piecewise function: if ¿, $f_{glucose}$=¿; if ¿, $f_{glucose}$=¿. Exponential decay and the Haldane-type inhibition term (Kang et al., 2016) were also tried for Eq. 6, but the performance was inferior to the piecewise function (**see Table S8 in SI**). Eq. 7 and Eq. 8 were both in the form of $\frac{v_{max} * k_1}{¿¿}$. The parameters in Eq. 6-8 were estimated by fitting these empirical functions to measured metabolite concentrations (**section 2.2**) and the computed cell-specific uptake rates of glucose, glutamine, and oxygen (**see section S1.1 and Figure S2 in SI**) using non-linear least squares regression (Vugrin et al., 2007) (**see Table S8 in SI**). As the growth medium contained abundant nutrient sources, there was no constraint on upper bounds of uptake fluxes of phosphate, bicarbonate, choline, and hypoxanthine.

$$Max\,\mu \quad (Eq.1)$$

$$Sv = 0 \quad (Eq.2)$$

Constrained allocation: $\phi_C + \phi_T + \phi_A + \phi_E + \phi_O (\geq \phi_{O,min}) = 100\,\% \quad (Eq.3)$

$$v_i \leq a_i [E_i] \forall\, i \in j, j = C, A, E, T \quad (Eq.4)$$

10

$$\sum_i \frac{v_{i\in j}}{a_{i\in j}} \le \phi_j * P_{TOT}, j = C, A, E, T \quad (Eq.5)$$

$$ub_{glucose} \le f_{glucose} ¿$$

$$ub_{glutamine} \le f_{glutamine} ¿$$

$$ub_{O_2} \le f_{O_2} ¿$$

To simulate the growth of *S. scrofa* muscle stem cells dynamically in a batch reactor, dynamic FBA (dFBA) was adopted, as a combination of FBA and differential-equation-based dynamic system modeling (Henson and Hanly, 2014). The concentration changes of extracellular metabolites ($[M_i]$) and *S. scrofa* muscle stem cell biomass ($[X]$) were modeled by differential equations to account for biomass accumulation (Eq. 9) and consumption/production of extracellular metabolites (Eq. 10). Because the growth rate of mammalian cells was relatively low, in comparison to microbial cells, a cell-specific death rate (k_d) was needed in dynamic FBA. k_d was set as 0.01/hr in this study (Xu et al., 2010). v_{EX_i} was the exchange flux of the extracellular metabolite M_i.

$$\frac{d[X]}{dt} = (\mu - k_d) * [X] \quad (Eq.9)$$

$$\frac{d[M_i]}{dt} = v_{EX_i} * [X] \quad (Eq.10)$$

3.Results

3.1 The effects of lactate and ammonium on *S. scrofa* muscle stem cells

To investigate the effects of accumulating lactate and ammonium (NH_4^+), *S. scrofa* muscle stem cells were cultured with two different initial NH_4^+ concentrations (1.073 +/- 0.021 mM and 3.823 +/- 0.015 mM) (**see Table S2&S3 in SI**). The biomass level could accumulate to 0.59 g/L in the low initial NH_4^+ level condition, which reduced to 0.39 g/L in the high initial NH_4^+

level condition (**Figure 1A**). For energy metabolism, the glucose and glutamine consumed and lactate produced in high initial NH_4^+ level condition were approximately half of those in low initial NH_4^+ level condition (**Figure 1BC**). The NH_4^+ concentration in the low initial NH_4^+ level condition was generally below 4mM, while that of high initial NH_4^+ level condition was generally above 4mM (**Figure 1C**). Therefore, lactate was likely the primary inhibitor of cellular growth under low initial NH_4^+ level conditions, whereas NH_4^+ was likely the primary inhibitor under high initial NH_4^+ level conditions. The computed growth rates of all time intervals showed that the stem cells were not fully activated before 42hr and 30hr for the low and high initial NH_4^+ level conditions, correspondingly (**Figure 1D**). Thereafter, the highest growth rates reached by stem cells in the low and high initial NH_4^+ conditions were 0.0664/hr and 0.0516/hr, correspondingly. Regarding the inhibitory effects of lactate and NH_4^+ on the growth rates of *S. scrofa* muscle stem cells, the negative Pearson correlations between lactate concentrations and growth rates in both culture conditions were not statistically significant, whereas NH_4^+ concentrations had significantly negative Pearson correlations with growth rates (**Figure 1EF**).

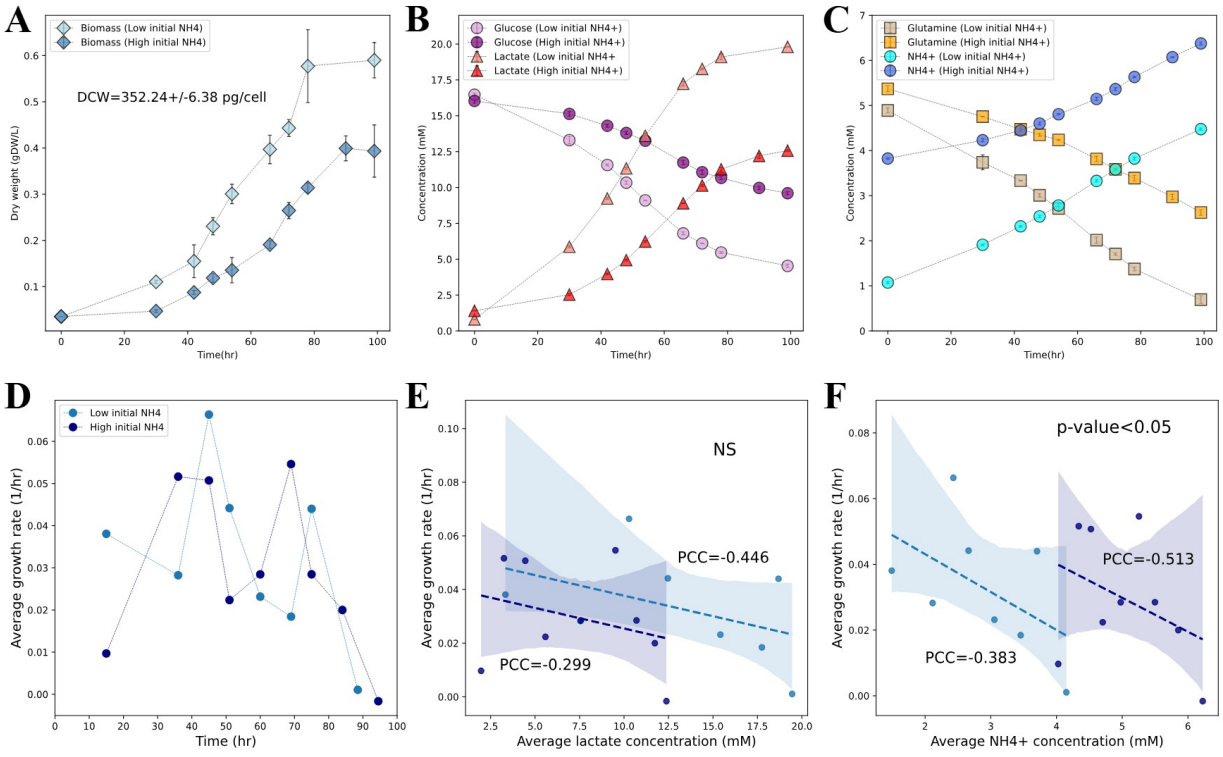

12

Figure 1. Growth and metabolism of *S. scrofa* muscle stem cells under low and high initial ammonium concentrations (1.073 +/- 0.021 mM and 3.823 +/- 0.015 mM). (A) Dry cellular biomass concentration profiles. DCW: dry cellular weight, DCW per cell = 352.24+/-6.38 pg/cell. (B) Concentration profiles of glucose and lactate. (C) Concentration profiles of glutamine and NH_4^+. (D) Average growth rates of all time intervals. (E) Pearson correlations between lactate concentrations and growth rates. (F) Pearson correlations between NH_4^+ concentrations and growth rates.

Cell-specific metabolic fluxes were computed based on biomass and metabolite concentrations to further quantify the metabolic status of *S. scrofa* muscle stem cells (**see section S1.1 and Figure S2 in SI**). To note, lactate:glucose and NH_4^+:glutamine molar ratios in this study represented the molar ratios of lactate production rate to glucose uptake rate and NH_4^+ production rate to glutamine uptake rate, respectively. The highest glucose uptake rates reached in low and high initial NH_4^+ conditions were 1.45 and 1.0322 mmol/gDW*hr, respectively (**Figure 2A**). In both culture conditions, the lactate:glucose molar ratios were around 1.75 at mid-exponential stage (excluding outliers), and then decreased to below 1.5 at late-exponential stage, indicating a carbon flux redirection from anaerobic fermentation of lactate to aerobic respiration (**Figure 2B**). The redirection of carbon flux from a low proteome cost pathway to a high proteome cost pathway (**Figure 3C**) implied that high lactate and NH_4^+ concentrations most likely inhibited the expression level of glycolysis rather than enzyme activities, as the reduction of glycolytic enzyme activities would raise the proteome cost of energy metabolism. The lactate:glucose molar ratios of the high initial NH_4^+ condition were slightly higher than those of the low initial NH_4^+ condition at mid- and late-exponential phases, suggesting a reduced energy yield from glucose due to the inhibition of oxidative phosphorylation by NH_4^+ (Ozturk et al., 1992). The highest glutamine uptake rates reached in low and high initial NH_4^+ conditions were 0.5266 and 0.4995 mmol/gDW*hr, respectively (**Figure**

13

2C). The NH_4^+:glutamine molar ratios were mostly fluctuating around 1 in both culture conditions, suggesting that glutamine metabolism was the major source of NH_4^+ production (**Figure 2D**). Subsequently, the quantitative relationships of lactate and NH_4^+ concentrations with glucose, glutamine, and oxygen uptake rates (OURs) were approximated based on metabolomics data with empirical functions (**see Table S8 in SI**) to model the inhibitory effects of lactate and NH_4^+ on glycolysis, amino acid metabolism, and oxidative phosphorylation (Chen et al., 2009; Cruz et al., 2000; Galvanauskas et al., 2019; Ozturk et al., 1992; Roon et al., 1975; Slivac et al., 2010) (**Figure 2E-G**). In short, experimental growth and metabolomics data quantitatively illustrated how accumulated lactate and NH_4^+ inhibited the growth and metabolism of *S. scrofa* muscle stem cells, contributing to metabolic flux simulation of *S. scrofa* muscle stem cells under varying culture conditions (**section 3.3**).

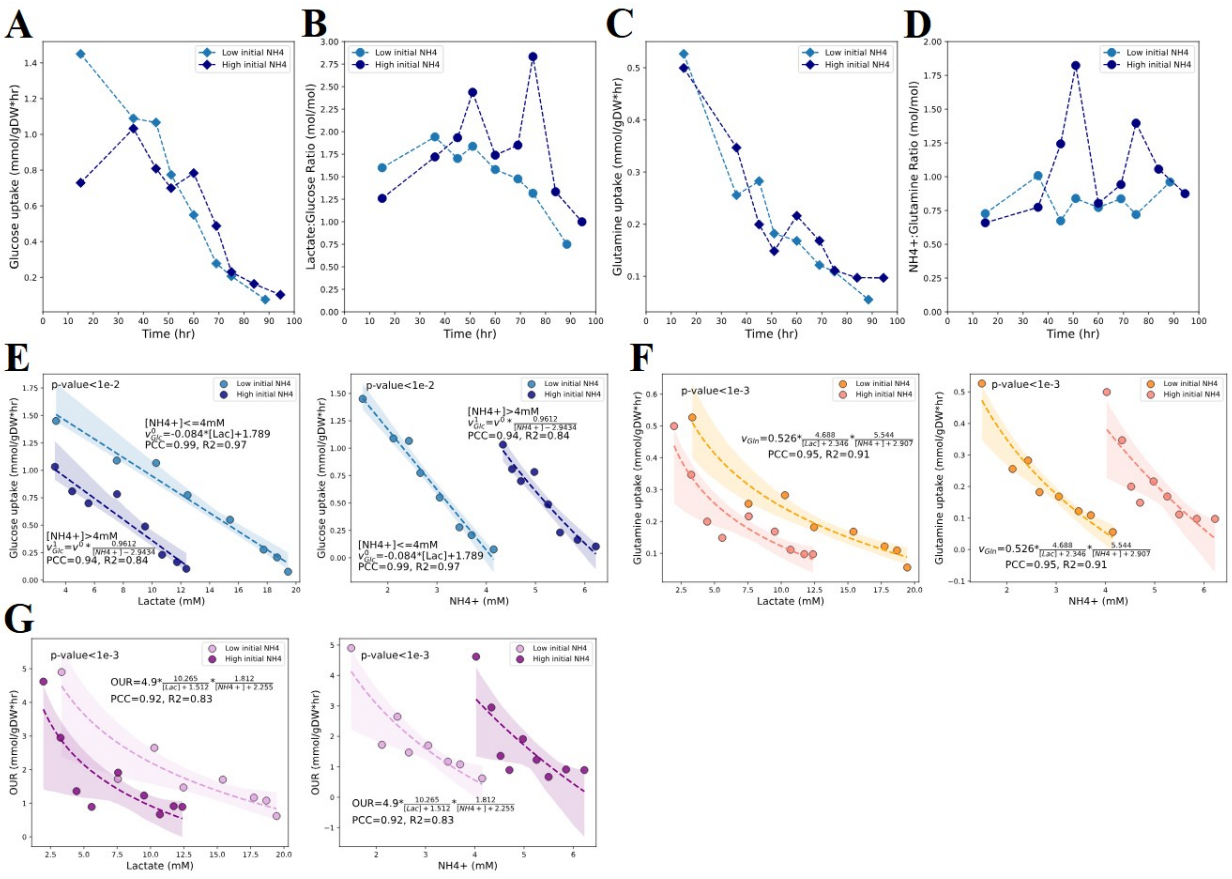

14

Figure 2. Experimental metabolic fluxes of *S. scrofa* muscle stem cells under low and high initial NH_4^+ level conditions. (A) Cell-specific glucose uptake rates. (B) Lactate: glucose molar ratios. (C) Cell-specific glutamine uptake rates. (D) NH_4^+:glutamine molar ratios. (E) The relationship between glucose uptake rates and lactate, NH_4^+ concentrations (p-value<0.01). (F) The relationship between glutamine uptake rates and lactate, NH_4^+ concentrations (p-value<0.001). (G) The relationship between oxygen uptake rates (OURs) and lactate, NH_4^+ concentrations (p-value<0.001).

3.2 Overview of the reduced metabolic model

The RMM of *S. scrofa* muscle stem cells, PigMNet2025, contains 504 reactions and 495 metabolites in total. Among 504 reactions, 82.3% have gene-protein-reaction rules, 7.3% are boundary reactions, and the rest 10.3% miss associated coding genes (**Figure 3A**). The top 5 subsystems (excluding exchange and transport) with most reactions are tyrosine metabolism, tryptophan metabolism, valine/leucine/isoleucine metabolism, glycolysis/gluconeogenesis, and glycine/serine/threonine metabolism (**Figure 3B**). However, flux variability analysis showed that a large fraction of reactions in tyrosine, tryptophan, valine/leucine/isoleucine, and glycine/serine/threonine metabolic pathways were not flux-active when amino acids were sufficiently supplied (**see Figure S7 in SI**), suggesting that the RMM could be further simplified for rich-medium settings. Among 495 metabolites, 314 are in cytoplasm, 144 are in mitochondrion, 37 are in extracellular space (**Figure 3C**). The quality of PigMNet2025 was assessed by MEMOTE (Lieven et al., 2020), and the overall consistency score was 97% (**see Table S4 in SI**). Subsequently, dry biomass composition of the *S. scrofa* muscle stem cell was measured to accurately model the biomass production rate (cellular growth rate) (**see section S1.2 in SI**). The average mass fractions of total protein, RNA, and DNA were 67.4%, 4.5%, and 1.1%, respectively (**Figure 3D**), and thus the total proteome mass (P_{TOT}) in Eq. 5 was set as 0.674

15

g/gDW. Molar ratios of amino acids in *S. scrofa* proteome (Müller et al., 2020) and deoxyribonucleic acids (dNTP) and ribonucleic acids (NTPs) in *S. scrofa* genome and transcriptome (Groenen et al., 2012) were used to estimate mass fractions of 20 essential amino acids, 4 dNTPs, and 4NTPs in dry cellular biomass (**Figure 3EF**). The details of biomass formation reaction can be found in **section S1.2 in SI**. The estimated GAM and NGAM values for low and high initial NH_4^+ level conditions were close, and this study adopted 93.8648 mmol/gDW and 2.2771 mmol/gDW*hr as the default GAM and NGAM values, respectively (**see Figure S3 in SI**). To sum up, PigMNet2025 is a RMM tailored for the core metabolism of *S. scrofa* muscle stem cells.

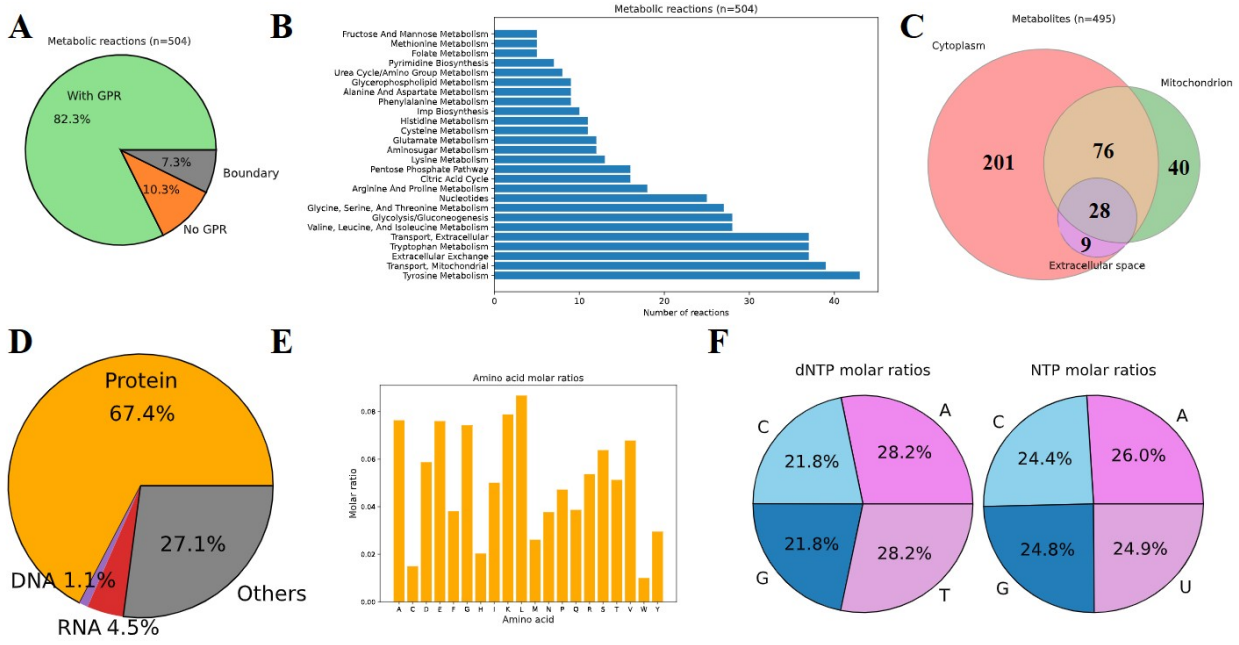

Figure 3. Overview of PigMNet2025. (A) Status of metabolic reaction curation, Green: reactions with GPR rules; Orange: reactions without GPR rules; Grey: exchange reactions at boundary. (B) Summary of curated metabolic reactions in different subsystems. (C) Summary of metabolites in different compartments. (D) Dry biomass composition of the *S. scrofa* stem cell. (E) Molar ratios of amino acids in the proteome of *S. scrofa*. (F) Molar ratios of deoxyribonucleic acids (dNTP) and ribonucleic acids (NTPs) in the genome and transcriptome of *S. scrofa*.

16

In order to build the proteome constrained FBA model of *S. scrofa* muscle stem cells, pcPigMNet2025 (**section 2.4**), enzyme activities were curated for all irreversible reactions (n=272) in PigMNet2025. 93 out of 272 enzyme activities were experimental data from *S. scrofa*, while the remaining enzyme activities were obtained from mammalian species genetically close to *S. scrofa* (e.g., *H. sapiens*) (**Figure 4A**). From curated enzyme activities in different pathways, glycolysis, pentose phosphate pathway, and TCA cycle were more efficient than most amino acid metabolic pathways (e.g., lysine metabolism) and biosynthetic pathways of DNA/RNA building blocks (e.g., pyrimidine biosynthesis) (**Figure 4B**). The integration of proteome costs defined by enzyme activities (**section 2.4**) enabled the modeling of lactate overflow at the exponential growth stage of mammalian cell cultures (Young, 2013). The lactate production pathway was much shorter than TCA cycle and oxidative phosphorylation, and the enzyme activity of lactate dehydrogenase (LDH) was higher than most enzymes in TCA cycle (**Figure 4C**). Therefore, due to the limitation of the proteome resource, the mammalian cell, even under aerobic condition, would favor lactate production in place of aerobic respiration to achieve higher metabolic efficiency, despite the greater ATP yield of aerobic respiration. Although using proteome efficiency to explain the overflow metabolism of mammalian cells remains controversial (Gosselin-Monplaisir et al., 2025; Y. Shen et al., 2024), Kukurugya et al., 2024 demonstrated that the anaerobic fermentation in *E. coli*, *S. cerevisiae*, and mammalian cells is more proteome-efficient in ATP yield than respiration (Kukurugya et al., 2024). Therefore, this study still adopted this theoretical model. Additionally, the relatively high activity of glutaminase (GLUNm) could explain why the mammalian cell would utilize glutamine as another major carbon source together with glucose (**Figure 4C**). Generally speaking, constrained proteome allocation could improve the performance of FBA by modeling the proteome resource coordination across different metabolic pathways.

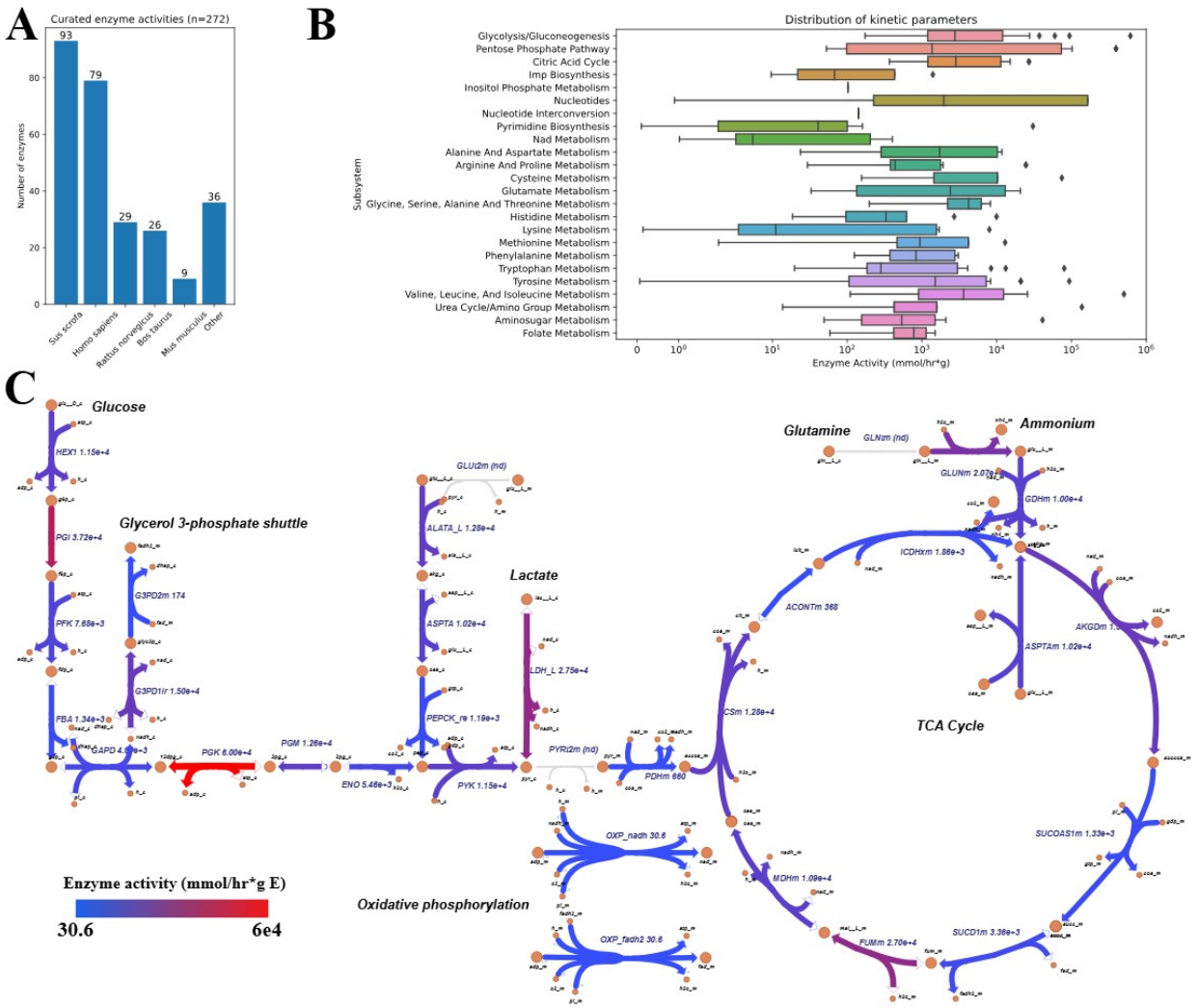

Figure 4. Enzyme specific activities of metabolic reactions in pcPigMNet2025. (A) Enzyme activities curated from *S. scrofa* and mammalian species close to *S. scrofa*. (B) Distribution of enzyme activities of metabolic reactions in different pathways. (C) Enzyme activities (mmol/hr per gram enzyme) mapped to the central carbon metabolic network (full names of reactions can be found in **SI, Table S5**).

18

3.3 Metabolic flux simulation of *S. scrofa* muscle stem cells under varying culture conditions

To examine the prediction performance of pcPigMNet2025, the static metabolic flux simulation was performed for experimental data from selected time intervals in low and high initial NH_4^+ level conditions (**Figure 5**). Details of experimental data for selected time intervals can be found in **SI, Table S7**. For the low initial NH_4^+ level condition, the simulation accurately predicted growth rates, glucose consumption rates, and lactate production rates (PCC>0.95, R2>0.7) (**Figure 5ABD**). While the prediction result captured the inhibition of glutamine metabolism by lactate and NH_4^+ (PCC>0.8), the quantitative accuracy of predicted glutamine consumption and NH_4^+ production rates was poor (R2<0) (**Figure 5CE**). Compared to the low initial NH_4^+ level condition, the predicted growth rates at high NH_4^+ concentrations were less quantitatively accurate (PCC<0.9, R2<0), suggesting that the inhibitory effect of NH_4^+ was not sufficiently well approximated (**Figure 5AF**). Similar to the low initial NH_4^+ level condition, the prediction of glucose consumption and lactate production rates was accurate (**Figure 5GI)**, but the prediction of glutamine consumption and NH_4^+ production rates could only capture the tendency (**Figure 5HJ**). For both low and high initial NH_4^+ condition, glutamine consumption rates were underestimated and NH_4^+:glutamine ratios were overestimated (**Figure 5CH**), indicating that the simulation overestimated the NH_4^+ production from the metabolic pathways of other amino acids (e.g., proline). Like glutamine, proline can also be converted to alpha-ketoglutarate by proline oxidase, 1-pyrroline-5-carboxylate dehydrogenase, and glutamate dehydrogenase (**see Figure S5 in SI**). Expectedly, inaccuracies in static metabolic flux simulations would propagate to dynamic metabolic flux simulations.

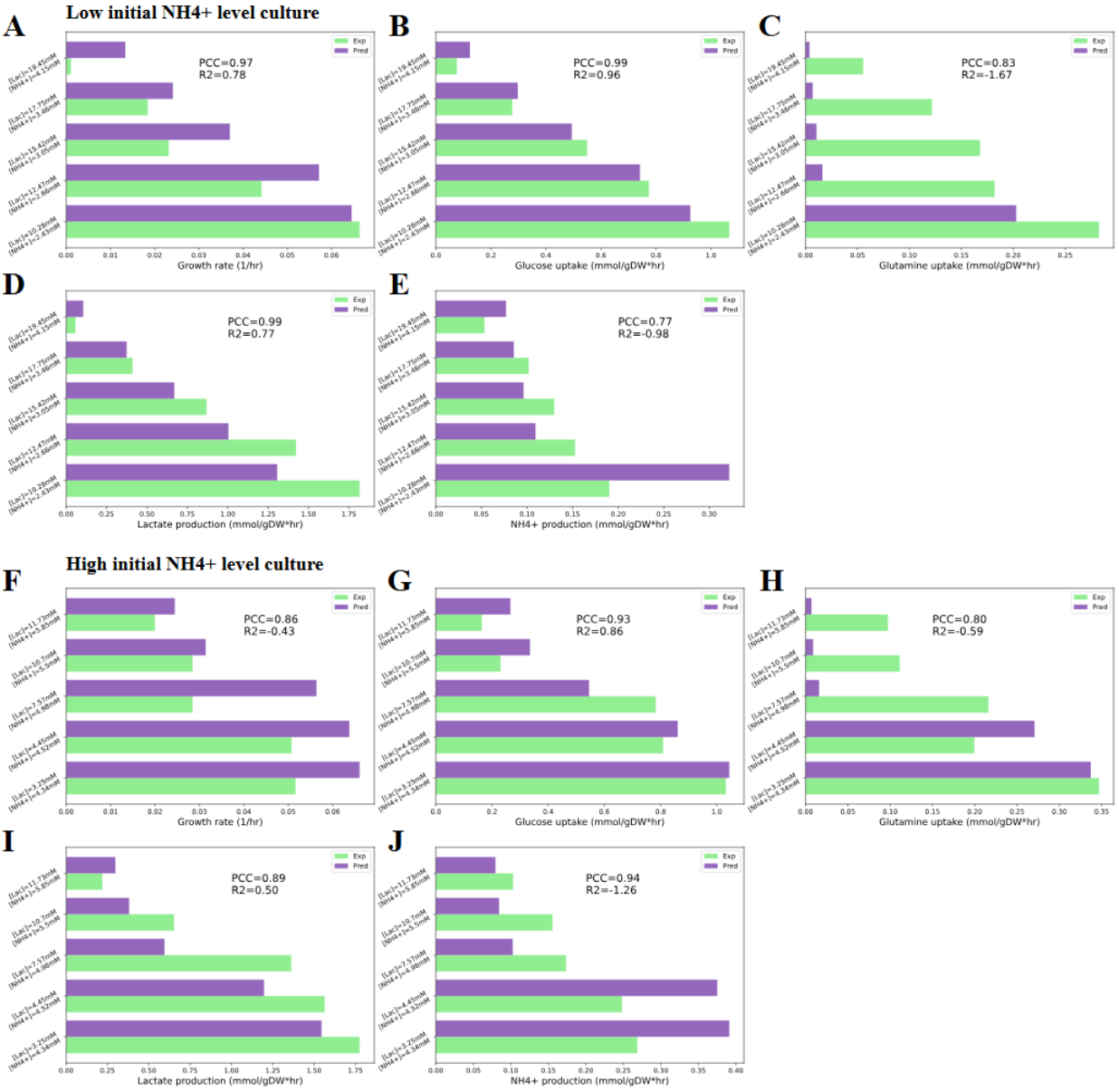

Figure 5. Static metabolic flux simulation for different lactate and NH_4^+ concentrations. A-E: low initial NH_4^+ level condition; F-J: high initial NH_4^+ level condition. (A) Experimental and predicted growth rates under low NH_4^+ level (Pearson correlation coefficient (PCC)=0.97). (B) Experimental and predicted glucose uptake rates under low NH_4^+ level (PCC=0.99). (C) Experimental and predicted glutamine uptake rates under low NH_4^+ level (PCC=0.83). (D) Experimental and predicted lactate production rates under low NH_4^+ level (PCC=0.99). (E) Experimental and predicted NH_4^+ production rates under low NH_4^+ level (PCC=0.77). (F)

20

Experimental and predicted growth rates under high NH_4^+ level (PCC=0.86). (G) Experimental and predicted glucose uptake rates under high NH_4^+ level (PCC=0.93). (H) Experimental and predicted glutamine uptake rates under high NH_4^+ level (PCC=0.80). (I) Experimental and predicted lactate production rates under high NH_4^+ level (PCC=0.89). (J) Experimental and predicted NH_4^+ production rates under high NH_4^+ level (PCC=0.94). Green: experimental data; Purple: prediction results.

The dynamic simulation of *S. scrofa* muscle stem cell proliferation was performed for both low and high initial NH_4^+ level conditions (**Figure 6**). Two initial conditions were: (1) T=42hr, [glucose]=11.567mM, [glutamine]=3.333mM, [lactate]=9.233mM, [NH_4^+]=2.320mM; (2) T=30hr, [glucose]=15.133mM, [glutamine]=4.753mM, [lactate]=2.533mM, [NH_4^+]=4.23mM (**see Table S1&S2 in SI**). For the low initial NH_4^+ level culture, the prediction result achieved good accuracy for the concentrations of biomass, glucose, lactate, and NH_4^+, but largely underestimated the consumption rate of glutamine (**Figure 6A-E**). For the high initial NH_4^+ level culture, the prediction result achieved good accuracy for the concentrations of biomass, glucose, glutamine, and NH_4^+, but underestimated the production rate of lactate (**Figure 6F-J**). The predicted growth curve of high initial NH_4^+ level culture was less accurate than that of low initial NH_4^+ level culture, suggesting that the characterization of the inhibition by NH_4^+ was not accurate enough (**Figure 6F**). The prediction result of high initial NH_4^+ level culture also underestimated the consumption rate of glutamine, although the quantitative accuracy was high before T=70hr (**Figure 6H**). In conclusion, pcPigMNet2025 can accurately predict growth kinetics and central carbon metabolism of *S. scrofa* muscle stem cells under varying lactate and NH_4^+ concentrations, but its quantitative accuracy on amino acid metabolism still requires improvement.

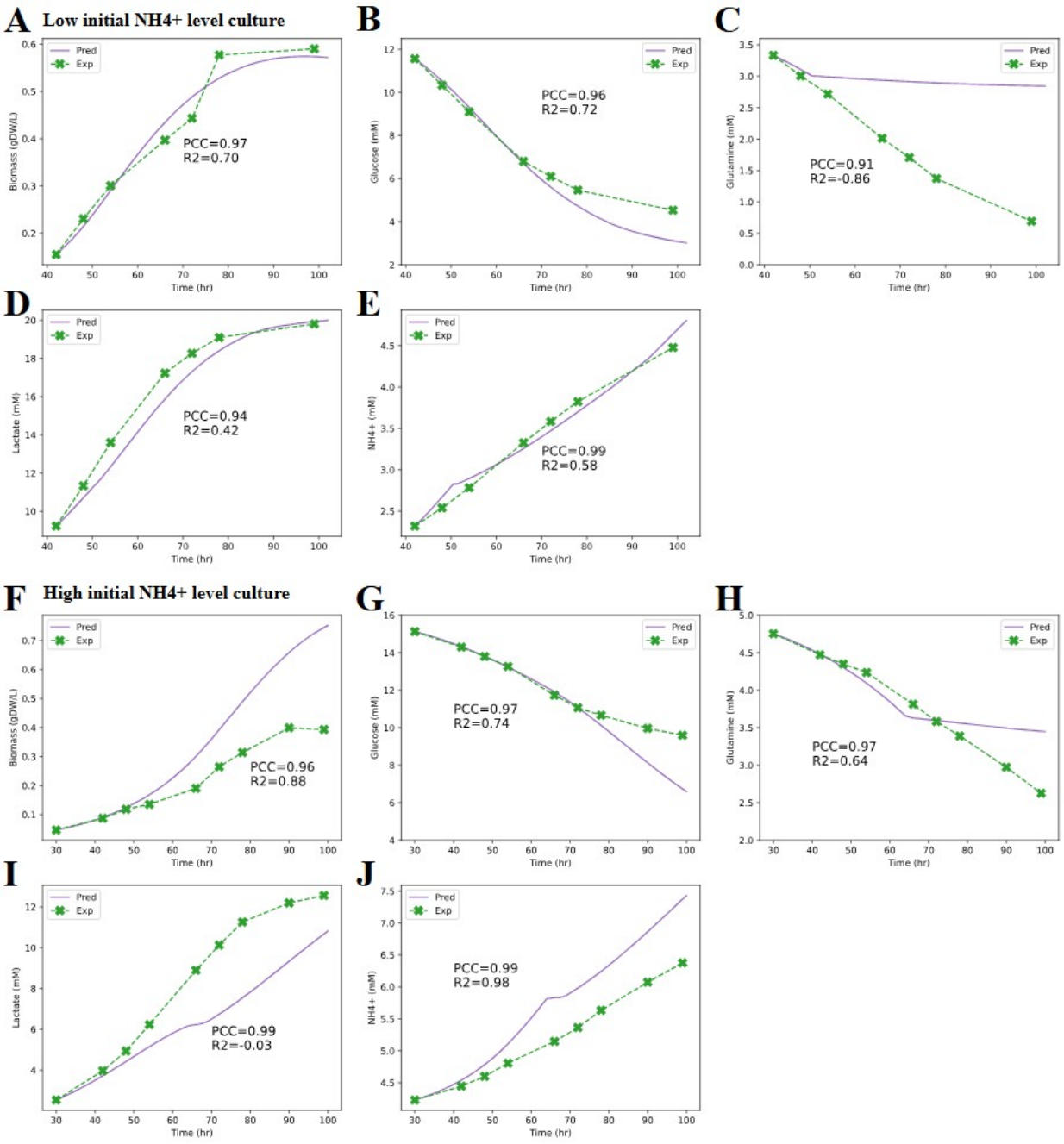

Figure 6. Dynamic simulation of *S. scrofa* muscle stem cell culture with low and high initial NH_4^+ concentrations. A-E: low initial NH_4^+ level, from 42hr to 100hr; F-J: high initial NH_4^+ level, from 30hr to 100hr. (A) Experimental and predicted biomass concentrations under low NH_4^+ level (Pearson correlation coefficient (PCC)=0.97). (B) Experimental and predicted glucose concentrations under low NH_4^+ level (PCC=0.96). (C) Experimental and predicted glutamine concentrations under low NH_4^+ level (PCC=0.91). (D) Experimental and predicted lactate

22

concentrations under low NH_4^+ level (PCC=0.94). (E) Experimental and predicted NH_4^+ concentrations under low NH_4^+ level (PCC=0.99). (F) Experimental and predicted biomass concentrations under high NH_4^+ level (PCC=0.96). (G) Experimental and predicted glucose concentrations under high NH_4^+ level (PCC=0.97). (H) Experimental and predicted glutamine concentrations under high NH_4^+ level (PCC=0.97). (I) Experimental and predicted lactate concentrations under high NH_4^+ level (PCC=0.99). (J) Experimental and predicted NH_4^+ concentrations under high NH_4^+ level (PCC=0.99). Green: experimental data; Purple: prediction results.

3.4 Perturbation simulation for non-growth associated maintenance and oxygen supply

Although the influence of accumulated lactate and NH_4^+ on NGAM was not observed in this study (**see Figure S3 in SI**), various types of environmental stress (e.g., osmotic pressure) in the bioreactor might affect the NGAM. Usually, the environmental stress will increase the NGAM (Kempes et al., 2017; Nakano et al., 2017; Varela et al., 2004). Therefore, a perturbation on NGAM values was performed, and ϕ_O was assumed to increase by the same fold changes (1.0 to 1.5) to reflect the proteome resource reallocation toward stress responses (**Figure 7A-C**). In the simulation, the increase of NGAM led to the decrease of growth rate from 0.0664/hr to 0.0083/hr due to the competition of energy and proteome resources between growth and stress responses (**Figure 7A**). The increase of lactate:glucose molar ratio reflected the inhibition of aerobic respiration, as the carbon flux through anaerobic fermentation of lactate increased (**Figure 7B**). The proteome resource reallocation toward stress responses limited the proteome resource available for central carbon metabolism, and thus inhibited aerobic respiration with a higher proteome cost than lactate production (**section 3.2**). At high NGAM, the glutamine metabolism was predicted to be the major source of NH_4^+ production, as glutamine can be

converted to a TCA cycle intermediate, alpha-ketoglutarate, with fewer steps than glucose (**Figure 7C**).

The oxygen supply is a limiting factor of cell proliferation in the bioreactor, and thus, this study also conducted a perturbation on cell-specific oxygen supply (**Figure 7D-F**). The simulation predicted that the increase of oxygen supply would increase the growth rate to 0.0664/hr, the maximum growth rate, and then the growth rate stayed unchanged (**Figure 7D**). The decrease of lactate:glucose ratio indicated the increase of the carbon flux fraction of aerobic respiration (**Figure 7E**), but the lactate:glucose ratio stopped decreasing after oxygen supply reached around 1.4 mmol/gDW*hr due to the limitation of the proteome resource (**section 3.2**). The fast drop of NH_4^+:glutamine ratio suggested that glutamine metabolism became the major source of NH_4^+ production at high oxygen supply (**Figure 7F**), because glutamine mainly participates in aerobic energy metabolism. The rapid redirection of carbon flux from anaerobic glycolysis to aerobic respiration when the oxygen supply increased from 1.3 to 1.35 mmol/gDW*hr (**Figure 7EF, Figure S8 in SI**) was driven by the activation of TCA cycle flux and the reallocation of proteome resources toward aerobic respiration. Comparable metabolic switches have been observed in the culture experiments of other eukaryotic cells (Martínez-Monge et al., 2019; Rodríguez-Torres et al., 2022). When the oxygen supply increased from 1.35 to 1.4 mmol/gDW*hr, the lactate:glucose ratio was predicted to rise and stabilize at 1.49 (**Figure 7E**), because the activation of glutamine catabolism reduced the carbon flux diverted from glycolysis to TCA cycle (**see Figure S8 in SI**). Similar transient metabolic responses have been reported in earlier FBA simulations and experimental studies (Erickson et al., 2017; Köbis et al., 2022; Yuan et al., 2024). In summary, these two perturbation case studies showed that pcPigMNet2025 could also model the effects of other environmental factors, beyond lactate and NH_4^+ stress.

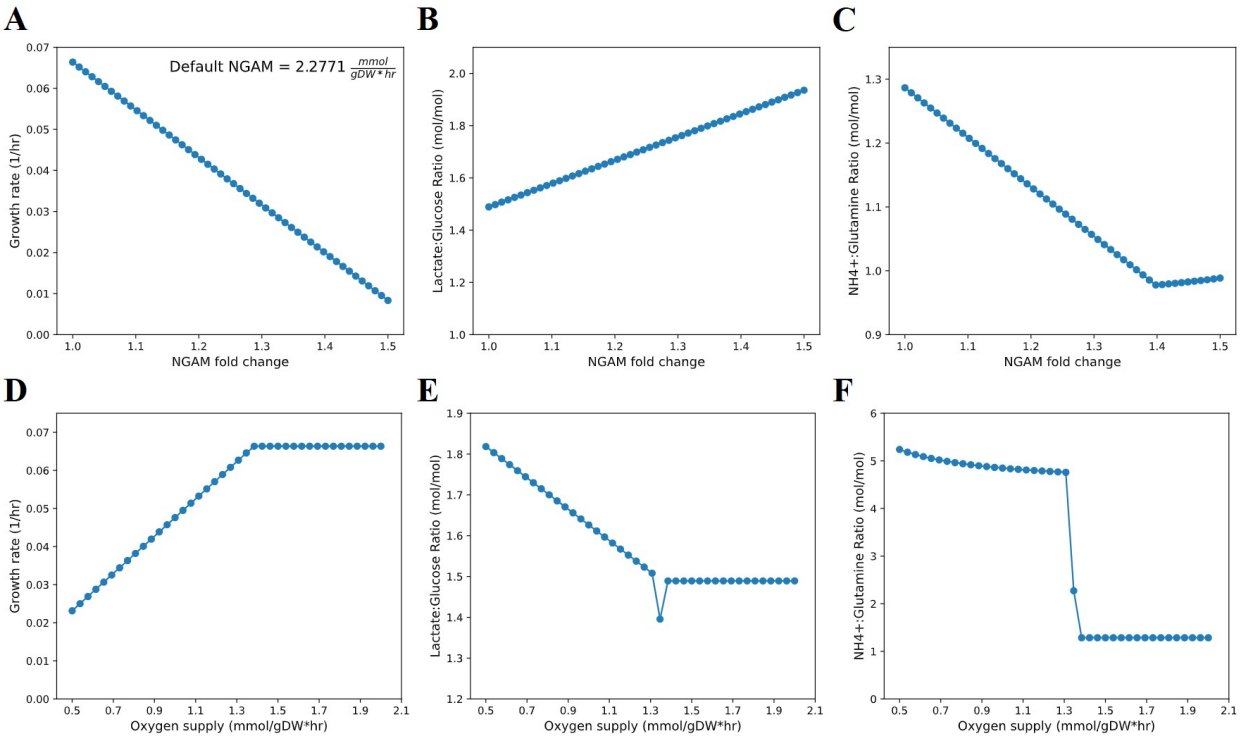

Figure 7. Perturbations on NGAM values and cell-specific oxygen supply levels. (A) Predicted growth rates with different NGAM fold changes. Default NGAM=2.2771 mmol/gDW*hr. (B) Predicted lactate:glucose molar ratios with different NGAM fold changes. (C) Predicted NH_4^+:glutamine molar ratios with different NGAM fold changes. (D) Predicted growth rates with different oxygen supply levels. (E) Predicted lactate:glucose molar ratios with different oxygen supply levels. (F) Predicted NH_4^+:glutamine molar ratios with different oxygen supply levels.

4.Discussion

Given the lack of a computational model for the proliferation of *S. scrofa* stem cells in cultured meat production, this study endeavored to construct a proteome constrained metabolic model named pcPigMNet2025 based on experimental growth and metabolomics data of *S. scrofa* stem cell culture under low and high initial NH_4^+ levels. The computed growth rates and metabolic fluxes allowed the quantification of the inhibitory effects of accumulated lactate and NH_4^+ on glycolysis, oxidative phosphorylation, and amino acid metabolism (**section 3.1**).

25

Subsequently, pcPigMNet2025, incorporating the effects of lactate and NH_4^+, adequately modeled the response of *S. scrofa* stem cells' metabolism to varying lactate and NH_4^+ concentrations (**section 3.3**). The validation with experimental data demonstrated that pcPigMNet2025 could accurately predict growth kinetics, glucose consumption, and lactate secretion. It could effectively capture the response of glutamine consumption and NH_4^+ secretion to changing concentrations of lactate and NH_4^+, although the quantitative accuracy remained to be improved. In addition, the perturbation simulation on NGAM and oxygen supply showed that pcPigMNet2025 could also account for other types of environmental stress (**section 3.4**). Briefly speaking, this study provided the first metabolic modeling framework for mammalian cells under environmental stress in actual bioprocesses.

Nonetheless, some limitations remained in the presented metabolic model. First, the evaluation of metabolic flux simulation found that the predicted growth rates at high NH_4^+ concentrations were less accurate than those at low NH_4^+ concentrations, and the primary error source was that the approximation of NH_4^+'s inhibitory effect was not accurate enough. Gene expression levels of *S. scrofa* muscle stem cells at different lactate and NH_4^+ concentrations allow the derivation of mathematical functions that describe proteome resource allocation induced by lactate and NH_4^+, which may improve the approximation of lactate's and NH_4^+'s inhibitory effects (Qiu et al., 2025). Another limitation was the overestimation of NH_4^+ production from the metabolic pathways of amino acids (e.g., arginine, leucine) other than glutamine, which was most likely caused by the inaccuracy of enzyme activity values (most of them were not specific to *S. scrofa*). The lack of organism-specific kinetic parameters was a well-acknowledged difficulty for proteome constrained metabolic modeling (Nilsson et al., 2017). Deep learning-based models have been developed to predict enzyme kinetic parameters, but the prediction error is not low enough (log10-scale RMSE=~0.8) to offer accurate parameter estimation (F. Li et al., 2022; Qiu et al., 2023b; X. Shen et al., 2024). Moreover, the stoichiometric coefficients of biomass components (e.g., 20 essential amino acids) in the

objective function (biomass formation) were estimated based on a coarse-grained biomass composition instead of precisely measured, resulting in uncertainty in modeling the growth and metabolism of *S. scrofa* muscle stem cells.

In spite of several limitations discussed above, pcPigMNet2025, presented in this study, exhibited the potential to be a model-aided process engineering tool for cultured meat production, which can be used to design optimal carbon/nitrogen source feeding strategies (Boojari et al., 2023) or co-culture of stem cells and probiotic *E. coli* strains to remove NH_4^+ (Kolodkin-Gal et al., 2024; Wassenaar, 2016). As envisaged, the accurate simulation of mammalian stem cells' growth and metabolism in bioreactors will give rise to the digital twin of cultured meat production, benefiting the development of future food.

Acknowledgements

This work was financially supported by Biotechnology and Biological Sciences Research Council of UK Research and Innovation (project ref. BB/Y007859/1). The authors thank Ivy Farm Technologies (Oxford, UK) and Julia Lee of Ivy Farm Technologies for their technical assistance with the experiments.

Author contributions

Sizhe Qiu conceptualized the study, developed the methodology, conducted experiments, performed data analysis, and contributed to the writing of the first draft. Eliska Kratochvilova contributed to methodology development, experimental work, and writing. Prof. Wei E. Huang, Prof. Zhanfeng Cui, and Dr. Tom Agnew assisted in the writing and review of the first draft. Prof. Aidong Yang and Prof. Hua Ye supervised this research project and critically reviewed the manuscript.

27

Conflict of Interest Statement

Prof. Hua Ye is the co-founder of Ivy Farm Technologies (Oxford, UK).

Data availability statement

The code and data are openly available at https://github.com/SizheQiu/PigMNet2025 and supplementary materials.

References

Boojari, M.A., Rajabi Ghaledari, F., Motamedian, E., Soleimani, M., Shojaosadati, S.A., 2023. Developing a metabolic model-based fed-batch feeding strategy for Pichia pastoris fermentation through fine-tuning of the methanol utilization pathway. Microb. Biotechnol. 16, 1344–1359.

Camacho, C., Coulouris, G., Avagyan, V., Ma, N., Papadopoulos, J., Bealer, K., Madden, T.L., 2009. BLAST+: architecture and applications. BMC Bioinformatics 10, 421.

Caro, D., Davis, S.J., Bastianoni, S., Caldeira, K., 2014. Global and regional trends in greenhouse gas emissions from livestock. Clim. Change 126, 203–216.

Chang, A., Jeske, L., Ulbrich, S., Hofmann, J., Koblitz, J., Schomburg, I., Neumann-Schaal, M., Jahn, D., Schomburg, D., 2021. BRENDA, the ELIXIR core data resource in 2021: new developments and updates. Nucleic Acids Res. 49, D498–D508.

Chen, T., Zhou, Y., Tan, W.-S., 2009. Influence of lactic acid on the proliferation, metabolism, and differentiation of rabbit mesenchymal stem cells. Cell Biol. Toxicol. 25, 573–586.

Cruz, H.J., Freitas, C.M., Alves, P.M., Moreira, J.L., Carrondo, M.J., 2000. Effects of ammonia and lactate on growth, metabolism, and productivity of BHK cells. Enzyme Microb. Technol. 27, 43–52.

Duarte, N.C., Becker, S.A., Jamshidi, N., Thiele, I., Mo, M.L., Vo, T.D., Srivas, R., Palsson,

B.Ø., 2007. Global reconstruction of the human metabolic network based on genomic and bibliomic data. Proc. Natl. Acad. Sci. U. S. A. 104, 1777–1782.

Ebrahim, A., Lerman, J.A., Palsson, B.O., Hyduke, D.R., 2013. COBRApy: COnstraints-Based Reconstruction and analysis for Python. BMC Syst. Biol. 7, 74.

Erickson, D.W., Schink, S.J., Patsalo, V., Williamson, J.R., Gerland, U., Hwa, T., 2017. A global resource allocation strategy governs growth transition kinetics of Escherichia coli. Nature 551, 119–123.

Galvanauskas, V., Simutis, R., Nath, S.C., Kino-Oka, M., 2019. Kinetic modeling of human induced pluripotent stem cell expansion in suspension culture. Regen. Ther. 12, 88–93.

Godfray, H.C.J., Aveyard, P., Garnett, T., Hall, J.W., Key, T.J., Lorimer, J., Pierrehumbert, R.T., Scarborough, P., Springmann, M., Jebb, S.A., 2018. Meat consumption, health, and the environment. Science 361. https://doi.org/10.1126/science.aam5324

Gosselin-Monplaisir, T., Enjalbert, B., Uttenweiler-Joseph, S., Portais, J.-C., Heux, S., Millard, P., 2025. Overflow metabolism in bacterial, yeast, and mammalian cells: different names, same game. Mol. Syst. Biol. 21, 1419–1433.

Groenen, M.A.M., Archibald, A.L., Uenishi, H., Tuggle, C.K., Takeuchi, Y., Rothschild, M.F., Rogel-Gaillard, C., Park, C., Milan, D., Megens, H.-J., Li, S., Larkin, D.M., Kim, H., Frantz, L.A.F., Caccamo, M., Ahn, H., Aken, B.L., Anselmo, A., Anthon, C., Auvil, L., Badaoui, B., Beattie, C.W., Bendixen, C., Berman, D., Blecha, F., Blomberg, J., Bolund, L., Bosse, M., Botti, S., Bujie, Z., Bystrom, M., Capitanu, B., Carvalho-Silva, D., Chardon, P., Chen, C., Cheng, R., Choi, S.-H., Chow, W., Clark, R.C., Clee, C., Crooijmans, R.P.M.A., Dawson, H.D., Dehais, P., De Sapio, F., Dibbits, B., Drou, N., Du, Z.-Q., Eversole, K., Fadista, J., Fairley, S., Faraut, T., Faulkner, G.J., Fowler, K.E., Fredholm, M., Fritz, E., Gilbert, J.G.R., Giuffra, E., Gorodkin, J., Griffin, D.K., Harrow, J.L., Hayward, A., Howe, K., Hu, Z.-L., Humphray, S.J., Hunt, T., Hornshøj, H., Jeon, J.-T., Jern, P., Jones, M., Jurka, J., Kanamori, H., Kapetanovic, R., Kim, J., Kim, J.-H., Kim, K.-W., Kim, T.-H., Larson, G., Lee,

568 K., Lee, K.-T., Leggett, R., Lewin, H.A., Li, Y., Liu, W., Loveland, J.E., Lu, Y., Lunney, J.K.,
569 Ma, J., Madsen, O., Mann, K., Matthews, L., McLaren, S., Morozumi, T., Murtaugh, M.P.,
570 Narayan, J., Nguyen, D.T., Ni, P., Oh, S.-J., Onteru, S., Panitz, F., Park, E.-W., Park, H.-S.,
571 Pascal, G., Paudel, Y., Perez-Enciso, M., Ramirez-Gonzalez, R., Reecy, J.M., Rodriguez-
572 Zas, S., Rohrer, G.A., Rund, L., Sang, Y., Schachtschneider, K., Schraiber, J.G., Schwartz,
573 J., Scobie, L., Scott, C., Searle, S., Servin, B., Southey, B.R., Sperber, G., Stadler, P.,
574 Sweedler, J.V., Tafer, H., Thomsen, B., Wali, R., Wang, J., Wang, J., White, S., Xu, X.,
575 Yerle, M., Zhang, G., Zhang, J., Zhang, J., Zhao, S., Rogers, J., Churcher, C., Schook,
576 L.B., 2012. Analyses of pig genomes provide insight into porcine demography and
577 evolution. Nature 491, 393–398.
578 Hassell, T., Gleave, S., Butler, M., 1991. Growth inhibition in animal cell culture. The effect of
579 lactate and ammonia. Appl. Biochem. Biotechnol. 30, 29–41.
580 Hefzi, H., Ang, K.S., Hanscho, M., Bordbar, A., Ruckerbauer, D., Lakshmanan, M., Orellana,
581 C.A., Baycin-Hizal, D., Huang, Y., Ley, D., Martinez, V.S., Kyriakopoulos, S., Jiménez,
582 N.E., Zielinski, D.C., Quek, L.-E., Wulff, T., Arnsdorf, J., Li, S., Lee, J.S., Paglia, G., Loira,
583 N., Spahn, P.N., Pedersen, L.E., Gutierrez, J.M., King, Z.A., Lund, A.M., Nagarajan, H.,
584 Thomas, A., Abdel-Haleem, A.M., Zanghellini, J., Kildegaard, H.F., Voldborg, B.G.,
585 Gerdtzen, Z.P., Betenbaugh, M.J., Palsson, B.O., Andersen, M.R., Nielsen, L.K., Borth, N.,
586 Lee, D.-Y., Lewis, N.E., 2016. A consensus genome-scale reconstruction of Chinese
587 hamster ovary cell metabolism. Cell Syst. 3, 434–443.e8.
588 Henson, M.A., Hanly, T.J., 2014. Dynamic flux balance analysis for synthetic microbial
589 communities. IET Syst. Biol. 8, 214–229.
590 Kang, S.-Y., Lee, S.-G., Kim, D.-J., Shin, J., Kim, J., Lee, S., Choi, J.-W., 2016. Comparison of
591 optimization algorithms for modeling of Haldane-type growth kinetics during phenol and
592 benzene degradation. Biochem. Eng. J. 106, 118–124.
593 Kempes, C.P., van Bodegom, P.M., Wolpert, D., Libby, E., Amend, J., Hoehler, T., 2017.

Drivers of bacterial maintenance and minimal energy requirements. Front. Microbiol. 8, 31.

King, Z.A., Dräger, A., Ebrahim, A., Sonnenschein, N., Lewis, N.E., Palsson, B.O., 2015. Escher: A Web Application for Building, Sharing, and Embedding Data-Rich Visualizations of Biological Pathways. PLoS Comput. Biol. 11, e1004321.

Köbis, M.A., Bockmayr, A., Steuer, R., 2022. Time-optimal adaptation in metabolic network models. Front. Mol. Biosci. 9, 866676.

Kolodkin-Gal, I., Dash, O., Rak, R., 2024. Probiotic cultivated meat: bacterial-based scaffolds and products to improve cultivated meat. Trends Biotechnol. 42, 269–281.

Kukurugya, M.A., Rosset, S., Titov, D.V., 2024. The Warburg Effect is the result of faster ATP production by glycolysis than respiration. Proc. Natl. Acad. Sci. U. S. A. 121, e2409509121.

Lee, J., Kim, J., Bae, H.W., Kim, M., Jung, B.K., Kim, J., Lee, S., Kim, H.U., 2024. Multi-omics analysis and genome-scale metabolic reconstruction of cattle*Bos taurus*for optimal production of cultured meat. bioRxiv. https://doi.org/10.1101/2024.12.09.627468

Lieven, C., Beber, M.E., Olivier, B.G., Bergmann, F.T., Ataman, M., Babaei, P., Bartell, J.A., Blank, L.M., Chauhan, S., Correia, K., Diener, C., Dräger, A., Ebert, B.E., Edirisinghe, J.N., Faria, J.P., Feist, A.M., Fengos, G., Fleming, R.M.T., García-Jiménez, B., Hatzimanikatis, V., van Helvoirt, W., Henry, C.S., Hermjakob, H., Herrgård, M.J., Kaafarani, A., Kim, H.U., King, Z., Klamt, S., Klipp, E., Koehorst, J.J., König, M., Lakshmanan, M., Lee, D.-Y., Lee, S.Y., Lee, S., Lewis, N.E., Liu, F., Ma, H., Machado, D., Mahadevan, R., Maia, P., Mardinoglu, A., Medlock, G.L., Monk, J.M., Nielsen, J., Nielsen, L.K., Nogales, J., Nookaew, I., Palsson, B.O., Papin, J.A., Patil, K.R., Poolman, M., Price, N.D., Resendis-Antonio, O., Richelle, A., Rocha, I., Sánchez, B.J., Schaap, P.J., Malik Sheriff, R.S., Shoaie, S., Sonnenschein, N., Teusink, B., Vilaça, P., Vik, J.O., Wodke, J.A.H., Xavier, J.C., Yuan, Q., Zakhartsev, M., Zhang, C., 2020. MEMOTE for standardized genome-scale metabolic model testing. Nat. Biotechnol. 38, 272–276.

Li, F., Yuan, L., Lu, H., Li, G., Chen, Y., Engqvist, M.K.M., Kerkhoven, E.J., Nielsen, J., 2022.

Deep learning-based kcat prediction enables improved enzyme-constrained model reconstruction. Nature Catalysis 1–11.

Li, M., Wang, D., Fang, J., Lei, Q., Yan, Q., Zhou, J., Chen, J., Guan, X., 2022. An efficient and economical way to obtain porcine muscle stem cells for cultured meat production. Food Res. Int. 162, 112206.

Martínez-Monge, I., Albiol, J., Lecina, M., Liste-Calleja, L., Miret, J., Solà, C., Cairó, J.J., 2019. Metabolic flux balance analysis during lactate and glucose concomitant consumption in HEK293 cell cultures: MARTÍNEZ-MONGE et al. Biotechnol. Bioeng. 116, 388–404.

Mori, M., Hwa, T., Martin, O.C., De Martino, A., Marinari, E., 2016. Constrained Allocation Flux Balance Analysis. PLoS Comput. Biol. 12, e1004913.

Müller, J.B., Geyer, P.E., Colaço, A.R., Treit, P.V., Strauss, M.T., Oroshi, M., Doll, S., Virreira Winter, S., Bader, J.M., Köhler, N., Theis, F., Santos, A., Mann, M., 2020. The proteome landscape of the kingdoms of life. Nature 582, 592–596.

Nakano, M., Imamura, H., Sasaoka, N., Yamamoto, M., Uemura, N., Shudo, T., Fuchigami, T., Takahashi, R., Kakizuka, A., 2017. ATP maintenance via two types of ATP regulators mitigates pathological phenotypes in mouse models of Parkinson's disease. EBioMedicine 22, 225–241.

Nilsson, A., Nielsen, J., Palsson, B.O., 2017. Metabolic models of protein allocation call for the kinetome. Cell Syst. 5, 538–541.

Nolan, R.P., Lee, K., 2011. Dynamic model of CHO cell metabolism. Metab. Eng. 13, 108–124.

Orth, J.D., Thiele, I., Palsson, B.Ø., 2010. What is flux balance analysis? Nat. Biotechnol. 28, 245–248.

Ozturk, S.S., Riley, M.R., Palsson, B.O., 1992. Effects of ammonia and lactate on hybridoma growth, metabolism, and antibody production. Biotechnol. Bioeng. 39, 418–431.

Post, M.J., 2012. Cultured meat from stem cells: challenges and prospects. Meat Sci. 92, 297–301.

Qiu, S., Yang, A., Yang, X., Ni, H., Li, W., Yang, Z., Zeng, H., Wang, Y., 2025. Proteome trade-off between primary and secondary metabolism shapes acid stress induced bacterial exopolysaccharide production. Metab. Eng. 91, 254–266.

Qiu, S., Yang, A., Zeng, H., 2023a. Flux balance analysis-based metabolic modeling of microbial secondary metabolism: Current status and outlook. PLoS Comput. Biol. 19, e1011391.

Qiu, S., Zhao, S., Yang, A., 2023b. DLTKcat: deep learning-based prediction of temperature-dependent enzyme turnover rates. Brief. Bioinform. 25. https://doi.org/10.1093/bib/bbad506

Rodríguez-Torres, M., Romo-Buchelly, J., Orozco-Sánchez, F., 2022. Effects of oxygen transfer rate on the L(+) lactic acid production by Rhizopus oryzae NRRL 395 in stirred tank bioreactor. Biochem. Eng. J. 187, 108665.

Roon, R.J., Larimore, F., Levy, J.S., 1975. Inhibition of amino acid transport by ammonium ion in Saccharomyces cerevisiae. J. Bacteriol. 124, 325–331.

Ryll, T., Valley, U., Wagner, R., 1994. Biochemistry of growth inhibition by ammonium ions in mammalian cells. Biotechnol. Bioeng. 44, 184–193.

Shen, X., Cui, Z., Long, J., Zhang, S., Chen, B., Tan, T., 2024. EITLEM-Kinetics: A deep-learning framework for kinetic parameter prediction of mutant enzymes. Chem Catal. 4, 101094.

Shen, Y., Dinh, H.V., Cruz, E.R., Chen, Z., Bartman, C.R., Xiao, T., Call, C.M., Ryseck, R.-P., Pratas, J., Weilandt, D., Baron, H., Subramanian, A., Fatma, Z., Wu, Z.-Y., Dwaraknath, S., Hendry, J.I., Tran, V.G., Yang, L., Yoshikuni, Y., Zhao, H., Maranas, C.D., Wühr, M., Rabinowitz, J.D., 2024. Mitochondrial ATP generation is more proteome efficient than glycolysis. Nat. Chem. Biol. 20, 1123–1132.

Shlomi, T., Benyamini, T., Gottlieb, E., Sharan, R., Ruppin, E., 2011. Genome-scale metabolic modeling elucidates the role of proliferative adaptation in causing the Warburg effect. PLoS Comput. Biol. 7, e1002018.

672 Slivac, I., Blajić, V., Radošević, K., Kniewald, Z., Gaurina Srček, V., 2010. Influence of different
673 ammonium, lactate and glutamine concentrations on CCO cell growth. Cytotechnology 62,
674 585–594.
675 Széliová, D., Ruckerbauer, D.E., Galleguillos, S.N., Petersen, L.B., Natter, K., Hanscho, M.,
676 Troyer, C., Causon, T., Schoeny, H., Christensen, H.B., Lee, D.-Y., Lewis, N.E.,
677 Koellensperger, G., Hann, S., Nielsen, L.K., Borth, N., Zanghellini, J., 2020. What CHO is
678 made of: Variations in the biomass composition of Chinese hamster ovary cell lines. Metab.
679 Eng. 61, 288–300.
680 Tullo, E., Finzi, A., Guarino, M., 2019. Review: Environmental impact of livestock farming and
681 Precision Livestock Farming as a mitigation strategy. Sci. Total Environ. 650, 2751–2760.
682 Varela, C.A., Baez, M.E., Agosin, E., 2004. Osmotic stress response: quantification of cell
683 maintenance and metabolic fluxes in a lysine-overproducing strain of Corynebacterium
684 glutamicum. Appl. Environ. Microbiol. 70, 4222–4229.
685 Vugrin, K.W., Swiler, L.P., Roberts, R.M., Stucky-Mack, N.J., Sullivan, S.P., 2007. Confidence
686 region estimation techniques for nonlinear regression in groundwater flow: Three case
687 studies. Water Resources Research 43. https://doi.org/10.1029/2005WR004804
688 Wagner-Golbs, A., Neuber, S., Kamlage, B., Christiansen, N., Bethan, B., Rennefahrt, U.,
689 Schatz, P., Lind, L., 2019. Effects of long-term storage at -80 °C on the human plasma
690 metabolome. Metabolites 9, 99.
691 Wang, H., Robinson, J.L., Kocabas, P., Gustafsson, J., Anton, M., Cholley, P.-E., Huang, S.,
692 Gobom, J., Svensson, T., Uhlen, M., Zetterberg, H., Nielsen, J., 2021. Genome-scale
693 metabolic network reconstruction of model animals as a platform for translational research.
694 Proc. Natl. Acad. Sci. U. S. A. 118, e2102344118.
695 Wassenaar, T.M., 2016. Insights from 100 years of research with probiotic E. coli. Eur. J.
696 Microbiol. Immunol. (Bp.) 6, 147–161.
697 Wittig, U., Rey, M., Weidemann, A., Kania, R., Müller, W., 2018. SABIO-RK: an updated

698 resource for manually curated biochemical reaction kinetics. Nucleic Acids Res. 46, D656–
699 D660.
700 Xu, X., Cowley, S., Flaim, C.J., James, W., Seymour, L., Cui, Z., 2010. The roles of apoptotic
701 pathways in the low recovery rate after cryopreservation of dissociated human embryonic
702 stem cells. Biotechnol. Prog. 26, 827–837.
703 Yang, J., Wang, Y., Fang, S., Qiang, Y., Liang, J., Yang, G., Feng, Y., 2020. Evaluation of
704 livestock pollution and its effects on a water source protection area in China. Environ. Sci.
705 Pollut. Res. Int. 27, 18632–18639.
706 Yeo, H.C., Hong, J., Lakshmanan, M., Lee, D.-Y., 2020. Enzyme capacity-based genome scale
707 modelling of CHO cells. Metabolic Engineering 60, 138–147.
708 Young, J.D., 2013. Metabolic flux rewiring in mammalian cell cultures. Curr. Opin. Biotechnol.
709 24, 1108–1115.
710 Yuan, H., Bai, Y., Li, X., Fu, X., 2024. Cross-regulation between proteome reallocation and
711 metabolic flux redistribution governs bacterial growth transition kinetics. Metab. Eng. 82,
712 60–68.
713 Zhu, H., Wu, Z., Ding, X., Post, M.J., Guo, R., Wang, J., Wu, J., Tang, W., Ding, S., Zhou, G.,
714 2022. Production of cultured meat from pig muscle stem cells. Biomaterials 287, 121650.